Neuron
Article

Cortical Feedback Control of Olfactory Bulb Circuits

Alison M. Boyd,[1,2] James F. Sturgill,[1,2] Cindy Poo,[1] and Jeffry S. Isaacson[1,*]
[1]Center for Neural Circuits and Behavior, Department of Neuroscience, University of California, San Diego, School of Medicine, La Jolla, CA 92093, USA
[2]These authors contributed equally to this work
*Correspondence: jisaacson@ucsd.edu
http://dx.doi.org/10.1016/j.neuron.2012.10.020

SUMMARY

Olfactory cortex pyramidal cells integrate sensory input from olfactory bulb mitral and tufted (M/T) cells and project axons back to the bulb. However, the impact of cortical feedback projections on olfactory bulb circuits is unclear. Here, we selectively express channelrhodopsin-2 in olfactory cortex pyramidal cells and show that cortical feedback projections excite diverse populations of bulb interneurons. Activation of cortical fibers directly excites GABAergic granule cells, which in turn inhibit M/T cells. However, we show that cortical inputs preferentially target short axon cells that drive feedforward inhibition of granule cells. In vivo, activation of olfactory cortex that only weakly affects spontaneous M/T cell firing strongly gates odor-evoked M/T cell responses: cortical activity suppresses odor-evoked excitation and enhances odor-evoked inhibition. Together, these results indicate that although cortical projections have diverse actions on olfactory bulb microcircuits, the net effect of cortical feedback on M/T cells is an amplification of odor-evoked inhibition.

INTRODUCTION

Cortical regions underlying vision, audition, and somatosensation receive sensory information from the thalamus and also make corticothalamic feedback projections that influence thalamic sensory processing (Briggs and Usrey, 2008; Cudeiro and Sillito, 2006). Thus, the cortex has the fundamental capacity to modulate the nature of its own input. In contrast to other sensory modalities, the olfactory system is unusual in that sensory information is initially processed in the olfactory bulb (OB) and conveyed directly (without a thalamic relay) to the olfactory cortex. Like the corticothalamic pathway, anatomical studies show that the axons of olfactory cortex pyramidal cells send abundant, long-range ''centrifugal'' projections back to the OB (de Olmos et al., 1978; Haberly and Price, 1978; Luskin and Price, 1983; Shipley and Adamek, 1984). However, functional properties of cortical feedback projections such as their neuronal targets, effects on local circuits, and impact on OB odor processing in vivo are poorly understood.

In the OB, principal mitral and tufted (M/T) cells belonging to unique glomeruli are activated by particular molecular features of individual odorants (Rubin and Katz, 1999; Soucy et al., 2009; Uchida et al., 2000). M/T cell output is strongly regulated by local GABAergic interneurons (Shepherd et al., 2004). Indeed, odors can elicit purely inhibitory M/T cell responses reflecting a major role for circuits mediating lateral inhibition in the OB (Cang and Isaacson, 2003; Davison and Katz, 2007; Yokoi et al., 1995). Reciprocal dendrodendritic synapses between M/T cell lateral dendrites and the distal dendritic spines of GABAergic granule cells (GCs) are the major source of recurrent and lateral inhibition of M/T cells and dendrodendritic inhibition triggered by M/T cell glutamate release is strongly dependent on the activation of GC NMDA receptors (NMDARs) (Chen et al., 2000; Isaacson and Strowbridge, 1998; Schoppa et al., 1998).

Sensory information from the OB is relayed via M/T cell axons within the lateral olfactory tract (LOT) directly to pyramidal cells in piriform cortex (PCx), a three-layered cortical region where bulbar inputs are integrated to form odor percepts (Haberly, 2001). Axon collaterals of PCx pyramidal cells provide excitatory projections back to the OB that are densest in the GC layer (Shipley and Adamek, 1984), suggesting that M/T cell inhibition is regulated by a long-range cortical feedback loop (Nakashima et al., 1978). In bulb-cortex slices, extracellular stimulation of PCx produced excitatory postsynaptic currents (EPSCs) in GCs and cortical input that drives GC action potentials (APs) is proposed to enhance M/T cell dendrodendritic self- and lateral inhibition (Balu et al., 2007; Halabisky and Strowbridge, 2003). This bulbo-cortical loop is also thought to contribute to oscillatory dynamics in the OB and cortex (Neville and Haberly, 2003) and proximal (presumptive cortical) inputs on GCs express long-term potentiation (LTP), suggesting they may play a role in olfactory learning (Gao and Strowbridge, 2009; Nissant et al., 2009). Furthermore, recordings in awake, behaving rodents show that M/T cell activity can be modulated by contextual information suggesting that higher cortical regions can influence odor processing in the OB (Kay and Laurent, 1999).

Despite the potential importance of cortical feedback in the regulation of OB circuits, the functional properties of these long-range projections are unclear. In large part, this reflects the challenge of selectively manipulating this feedback pathway using conventional extracellular electrical stimulation since

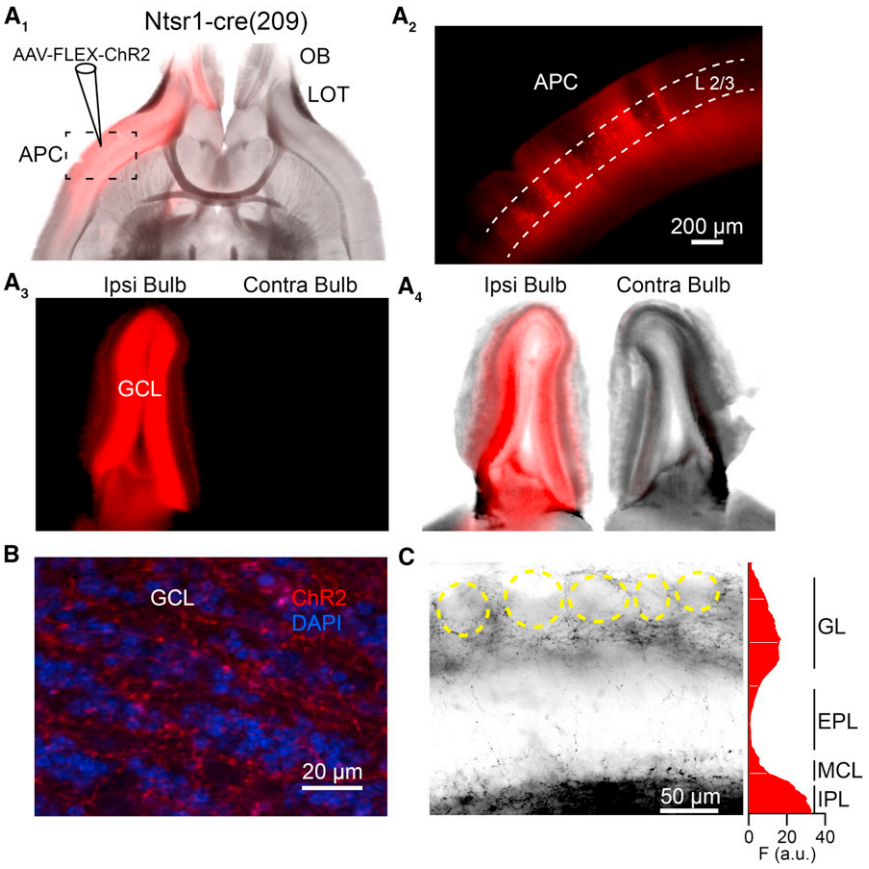

Figure 1. Conditional Expression of ChR2 in Piriform Cortex Pyramidal Cells Reveals Cortical Feedback Projections to the Olfactory Bulb

(A_1) Overlay of bright-field and fluorescence (red) image of a horizontal section (300 μm) of forebrain from an Ntsr1-cre mouse showing ChR2-mCherry expression in olfactory cortex. APC, anterior piriform cortex; LOT, lateral olfactory tract; OB, olfactory bulb. (A_2) Blow-up of region in (A_1) indicating expression of ChR2 in layer 2/3 pyramidal cells. (A_3) ChR2 is expressed in the ipsilateral, but not contralateral OB from the same mouse. GCL, granule cell layer. (A_4) Overlay of fluorescence and bright field images of the bulbs.

(B) Two-photon image (30 μm z-projection) of ChR2-mCherry in the GCL of a slice counterstained with DAPI.

(C) Left: gray-scale fluorescence image of ChR2-mCherry (black) in a slice (300 μm) indicating few fibers in the mitral cell layer (MCL) and external plexiform layer (EPL), but numerous fibers and varicosities surrounding glomeruli (yellow circles). Right: average fluorescence intensity (F, arbitrary units) along the vertical axis of the image. GL, glomerular layer; IPL, internal plexiform layer.

cortical fibers are intermingled with the axons and dendrites of bulbar neurons. In this study, we express channelrhodopsin-2 (ChR2) selectively in olfactory cortex pyramidal cells and examine the impact of cortical feedback on circuits in OB slices and its actions on odor-evoked activity in vivo.

RESULTS

We took advantage of a transgenic mouse line (Ntsr1-creGN209 from the GENSAT project) that expresses Cre recombinase in olfactory cortex pyramidal cells, but not in pyramidal cells of other cortical regions or in inhibitory interneurons (Experimental Procedures) (Stokes and Isaacson, 2010). We injected the anterior PCx of neonatal mice with an adeno-associated virus (AAV-double floxed-ChR2-mCherry) to drive Cre-dependent co-expression of the light-activated channel ChR2 (Atasoy et al., 2008; Petreanu et al., 2009) and the fluorescent protein mCherry. We chose this conditional strategy since injections of unconditional AAV-ChR2 could reach the lateral ventricle, leading to ChR2 expression in OB interneurons of wild-type mice (not shown). With this conditional approach, unilateral injections labeled layer 2/3 pyramidal cells in PCx and fibers that projected rostrally (Figures 1A_1 and 1A_2). Consistent with anatomical studies of the axonal projections of PCx pyramidal cells (Matsutani, 2010; Shipley and Adamek, 1984), expression of ChR2-mCherry was present in the ipsi- but not contralateral OB with the densest labeling in the GC layer and lesser expression in the glomerular layer (Figures 1A_3 and 1A_4). Two-photon imaging of the GC layer confirmed that ChR2 was present only in fibers and axonal varicosities (Figure 1B) rather than cell bodies of OB neurons. Consistent with tracing studies of the axonal trajectories of PCx pyramidal cells (Matsutani, 2010), we observed only scattered expression of ChR2-expressing fibers in the EPL, yet fibers and varicosities were found to surround but not extend into glomeruli (Figure 1C). Pyramidal cells of the anterior olfactory nucleus (AON, the most rostral region of olfactory cortex) project to both ipsi- and contralateral OBs, however, only rarely (5/39 injections) did we observe labeled fibers in the anterior pole of the anterior commissure or contralateral OB. Together, these results indicate that we can exclusively express ChR2 in long-range axonal projections within the OB that predominantly arise from PCx.

Cortical Feedback Drives Disynaptic Inhibition of Mitral Cells

We first examined the influence of cortical feedback projections on mitral cells by activating ChR2-expressing cortical fibers in OB slices using brief (1–4 ms) flashes of blue light. In mitral cells voltage-clamped at the reversal potential for EPSCs (V_m = 0 mV), light flashes elicited inhibitory postsynaptic currents (IPSCs) (Figure 2A) that were abolished by the $GABA_A$ antagonist gabazine (10 μM, n = 5; Figure 2A_2). Light-evoked mitral cell IPSCs were unaffected by application of the NMDAR antagonist APV alone (100 μM, 97 ± 9% of control, n = 4) but completely blocked in the presence of the AMPA receptor (AMPAR) antagonist NBQX (20 μM, 1.2 ± 0.7% of control, n = 11; Figure 2A_3). Thus,

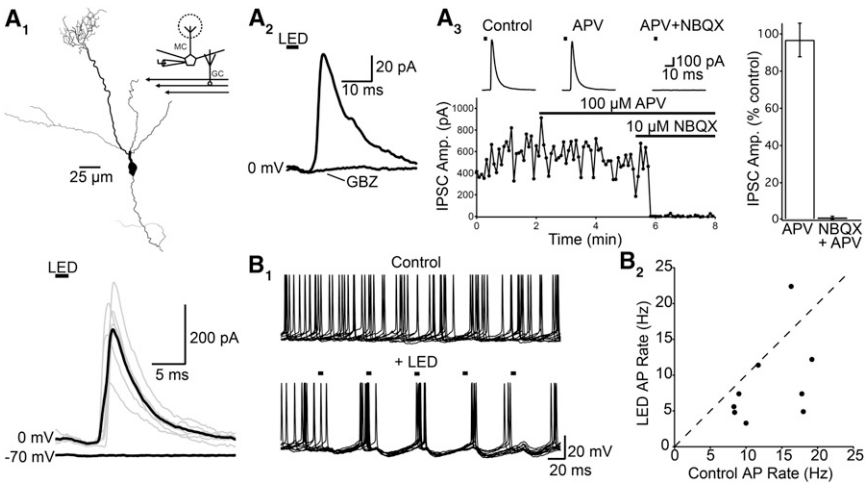

Figure 2. Cortical Feedback Drives Disynaptic Inhibition of Mitral Cells

(A_1) Anatomical reconstruction (top) and voltage clamp recording (bottom) of a mitral cell. Brief LED flashes (4 ms, black bar) evoke IPSCs at 0 mV (gray, individual trials; black, average). Inset: recording schematic. (A_2) Light-evoked IPSCs are blocked by gabazine (GBZ, 10 μM). (A_3) Light-evoked IPSCs are driven by AMPARs. Left: time course of one experiment (bottom) and traces (top) showing that the IPSC is unaffected by APV (100 μM) but abolished following subsequent application of NBQX (10 μM). Right: summary of the effects of APV alone (n = 4) and coapplication of APV and NBQX (n = 11) on IPSCs.

(B_1) Disynaptic IPSPs can reduce mitral cell firing. Current clamp recordings of a mitral cell depolarized to fire APs under control conditions (top) and on interleaved trials with a train of LED flashes (5 pulses, 20 Hz). Ten trials superimposed for each condition. (B_2) Summary of the effects of light-evoked IPSPs (LED AP Rate) on firing (Control AP rate, n = 9 cells). Each point represents one cell. Error bars represent SEM. See also Figure S1.

activation of cortical fibers elicits indirect inhibition of mitral cells that is mediated by AMPAR-driven excitation.

We next recorded from mitral cells in current clamp to determine the effects of cortical inputs on cell excitability. We depolarized cells (V_m = −51.3 ± 2.6 mV, n = 9) so that they were suprathreshold for firing APs and interleaved control trials with those containing a train of light flashes (five pulses, 20 Hz; Figure 2B_1). The desensitization properties of ChR2 precluded using higher stimulus frequencies (Petreanu et al., 2009). Individual light-evoked inhibitory postsynaptic potentials (IPSPs, first flash −5.0 ± 0.8 mV, last flash −4.9 ± 0.6 mV) transiently suppressed AP firing while the decay of the IPSP led to rebound firing (78 ± 48% increase in APs relative to control trials, 15 ms time window). These effects are consistent with previous studies showing that brief membrane hyperpolarization generates rebound APs in mitral cells (Balu and Strowbridge, 2007; Desmaisons et al., 1999). We compared the firing rate with and without activation of cortical fibers over the time period coinciding with the onset of the train of flashes to 50 ms after the last flash. Although the firing rate of most cells (7/9) was reduced by activation of cortical fibers (Figure 2B_2), other cells (2/9) showed no change or an increase in firing rate due to rebound spikes triggered by IPSPs.

We did not detect evidence for conventional fast excitatory synaptic responses elicited by photoactivation of cortical fibers in mitral cells, however, we observed small inward currents (average amplitude 15.1 ± 3 pA, V_m = −80 mV, n = 19) that preceded the onset of IPSCs (by 3.6 ± 0.6 ms, n = 6) and persisted in the presence of $GABA_A$ blockers (gabazine, 10 μM or picrotoxin, 100 μM). These evoked currents were blocked by NBQX (12.9 ± 4.5% of control, n = 5) but had unusual properties including slow kinetics (10%–90% rise time 6.7 ± 0.9 ms, decay τ 36.3 ± 1.1 ms, n = 19), virtually no trial-to-trial amplitude variability (coefficient of variation 0.05 ± 0.01, n = 19), and little sensitivity to membrane potential (7.5 ± 2.7% reduction in amplitude from −80 mV to −40 mV, n = 7) (Figure S1 available online). These responses were also observed in cells in which the primary apical dendrite was severed (n = 3). Although we cannot rule out the possibility that these small responses reflect synaptic contacts that only occur onto electrotonically remote regions of lateral dendrites or axons, they could also reflect glutamate spillover from cortical fibers onto distal processes, intracellular detection of local field potentials, or gap junctional coupling with cells receiving direct synaptic input. Regardless of their exact origin, these small currents did not have an obvious effect on mitral cell excitability since they caused only weak membrane depolarization (0.3 ± 0.1 mV at rest, n = 9) and never elicited APs.

Cortical Feedback Drives Direct Excitation and Feedforward Inhibition of Granule Cells

Granule cells are thought to be the major target of direct excitation from cortical feedback projections (Strowbridge, 2009). Indeed, brief light flashes evoked EPSCs in GCs (Figure 3A_1) with fast kinetics (10%–90% rise time: 0.76 ± 0.06 ms, decay τ: 1.49 ± 0.08 ms, amplitude range:13 to 587 pA, n = 20) and little jitter in their onset times (SD = 0.23 ± 0.02 ms, n = 20). Light-evoked EPSCs in GCs were abolished by tetrodotoxin (TTX, 1 μM, n = 6) but were partially recovered following subsequent application of the K^+ channel blocker 4-aminopyridine (4-AP, 1 mM, n = 5; Figure 3A_2). Consistent with previous studies (Petreanu et al., 2009), the synaptic response elicited in the presence of TTX and 4-AP indicates that we could trigger transmission via direct ChR2-mediated depolarization of boutons, however, the responses we observe under normal conditions reflect AP-mediated transmitter release from cortical fibers. Membrane depolarization (V_m = +40 mV) in the presence of picrotoxin (100 μM) revealed a slow NMDAR component to cortically-driven EPSCs that was abolished by APV (n = 4), while the fast EPSCs were blocked by NBQX (n = 7, Figure 3A_3). The current-voltage relationship of the isolated AMPAR response was linear (n = 5; Figure 3A_4), indicating that AMPARs at cortical synapses on GCs are Ca^{2+}-impermeable (Hollmann and Heinemann, 1994).

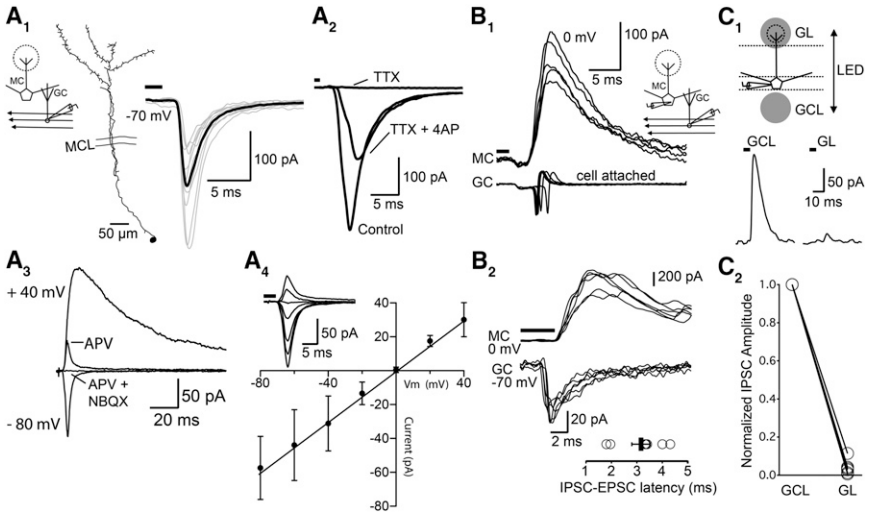

Figure 3. Cortical Feedback Directly Excites GCs

(A_1) Anatomical reconstruction (left) and voltage clamp recording (V_m = −70 mV) (right) of a GC receiving light-evoked EPSCs. Bar, LED illumination. MCL, mitral cell layer. Inset: recording schematic. (A_2) Light-evoked GC EPSCs are blocked by TTX (1 μM) and partially recovered by application of 4-AP (1 mM). (A_3) EPSCs have both AMPAR and NMDAR components. In the presence of picrotoxin (100 μM), depolarization to +40 mV reveals a slow current blocked by APV (100 μM). Subsequent addition of NBQX (20 μM) abolishes the fast EPSC. (A_4) Current-voltage relationship of the AMPAR EPSC (in the presence of APV) is linear (n = 5 cells). Inset: EPSCs from a representative cell. (B_1) Simultaneous voltage clamp recording of a mitral cell (0 mV) and cell-attached recording of a GC show that light-evoked GC APs overlap with mitral cell inhibition. (B_2) Simultaneous voltage clamp recording of a mitral (0 mV) and granule (−70 mV) cell reveal that the onset of cortically-driven EPSCs precedes that of mitral cell IPSCs. *Bottom*, IPSC-EPSC latencies (n = 7 cell pairs). (C_1) Recording schematic (top) and light-evoked responses from a mitral cell (bottom, 0 mV) when illumination was directed to the GC layer (GCL) or the glomerular layer (GL). (C_2) Summary data (n = 6 cells) shows that shifting photostimulation to the glomerular layer reduces the amplitude of light-evoked IPSCs. Error bars represent SEM.

We think it likely that GCs are a major source of cortically-evoked disynaptic inhibition onto mitral cells. Cell-attached recordings of GCs revealed that cortical input is sufficient to drive GCs to spike threshold (n = 5; Figure 3B_1). Furthermore, simultaneous whole-cell recordings indicated that the onset of evoked mitral cell IPSCs followed EPSCs in GCs with a disynaptic latency (3.2 ± 0.4 ms, n = 7; Figure 3B_2). We also tested the relative contribution of glomerular layer interneurons to mitral cell inhibition. LED illumination was restricted to a spot (~150 μm diameter) and we compared the amplitude of IPSCs elicited when the photostimulus was over the GC layer versus when the illumination surrounded the glomerulus containing the dendritic tuft of the recorded mitral cell (filled with fluorescent indicator). Shifting the location of the photostimulus from the GC layer to the glomerular layer largely abolished light-evoked mitral cell IPSCs (Figure 3C; 4.0 ± 1.6% of GC layer response, n = 6), indicating that cortically-evoked mitral cell inhibition arises primarily from the GC layer. Taken together, these results are consistent with the idea that activation of cortical fibers is sufficient to elicit disynaptic inhibition onto mitral cells that results from AMPAR-mediated excitation of GCs.

Intriguingly, activation of cortical feedback projections also elicited feedforward IPSCs in GCs. $GABA_A$R-mediated IPSCs (recorded at the reversal potential for excitation) followed light-evoked EPSCs with a disynaptic delay (3.5 ± 0.5 ms, n = 14; Figures 4A_1 and 4A_2) and were abolished following application of glutamate receptor antagonists (Figure 4A_3). Short-latency feedforward inhibition plays an important role in regulating time windows for excitation (Pouille and Scanziani, 2001). Indeed, in current clamp recordings (V_m = −60 mV) of cells with a mixed EPSP-IPSP, blocking the disynaptic IPSP greatly prolonged the duration of cortically-evoked EPSPs (½ width = 6.5 ± 1.7 ms versus 58.4 ± 18.7 before and after gabazine, respectively) without effecting peak EPSP amplitude (110.4 ± 7.7% of control, n = 5, Figure 4B). Although the amplitudes of light-evoked excitatory and inhibitory conductances were similar across the population of recorded GCs (average excitation [GE] = 1.1 ± 0.3 nS, inhibition [GI] = 1.4 ± 0.3 nS, n = 42), the relative contribution of inhibition to the total conductance (GI/(GE + GI)) varied widely within individual cells (Figure 4C). Anatomical reconstruction of dye-filled GCs did not reveal an obvious correlation between cell morphology and the excitation/inhibition ratio (n = 7, data not shown). Heterogeneity in the relative amount of excitation versus inhibition received by individual GCs suggests that cortical feedback inputs could have diverse effects: activation of the same cortical fibers could cause a net increase in the excitability of some GCs while neighboring GCs are suppressed. We tested this idea by giving nearby (within 100 μm) GCs depolarizing current steps sufficient to elicit APs and interleaving trials with and without trains of light flashes. Indeed, we found that cortical fiber activation in the same region could either enhance or suppress AP firing in GCs (Figure 4D_1). Although the majority of cells receiving light-evoked input responded with net excitation (7/12 cells, three slices), net inhibition was also observed (4/12 cells; Figure 4D_2). Together, these results indicate that in addition to direct excitation, cortical projections drive feedforward inhibition of GCs and that the net effect of cortical input on individual GCs can vary between excitation and inhibition.

Cortical Feedback Projections Preferentially Target Short Axon Cells

What circuit underlies cortically-evoked feedforward inhibition of GCs? Deep short axon cells (dSACs) in the GC layer are a heterogeneous class of GABAergic interneurons that mediate interneuron-selective inhibition: EM analysis indicates that dSAC terminals target GC dendrites but do not form synaptic contacts

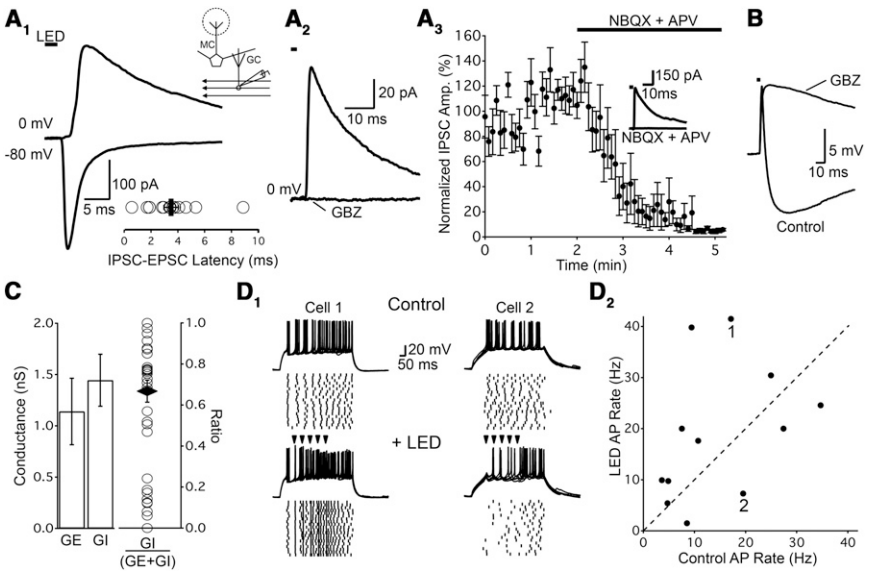

Figure 4. Cortical Feedback Drives Disynaptic Feedforward Inhibition of GCs

(A_1) GC voltage clamp recording illustrating a light-evoked EPSC (−80 mV) and short-latency IPSC (0 mV). Inset: latency between the IPSC and EPSC onset (circles, n = 14 cells; bar, mean). (A_2) Light-evoked IPSCs (V_m = 0 mV) in GCs are abolished by gabazine (10 μM, GBZ). (A_3) IPSCs are abolished by glutamate receptor antagonists (NBQX, 10 μM and APV, 100 μM, n = 8). Inset: responses from a representative cell (V_m = 0 mV).

(B) Current clamp recording of a GC (−60 mV) showing that disynaptic inhibition limits the time course, but not the amplitude of the cortically-evoked EPSP.

(C) Left: average inhibitory (GI) and excitatory (GE) conductances in the same cells (n = 42) evoked by photostimulation. Right: GI relative to total conductance was highly variable across individual cells (circles: individual cells; black diamond: mean ± SEM). Only cells with GI or GE >0.5 nS are included.

(D_1) Photoactivation of cortical fibers can lead to net increases or decreases in excitability in neighboring GCs. Traces show superimposed responses (five consecutive trials) to depolarizing current injection (50 pA) on interleaved trials with (+LED) and without (Control) a train of 5 light pulses at 20 Hz (arrowheads). Rasters show APs for 20 trials. Cell 1 responded to activation of cortical fibers with an increase in firing during the LED train whereas Cell 2 showed a decrease in firing. (D_2) AP rate of cells (n = 12) measured during the train of LED stimuli show that cortical input increased firing in the majority of cells whereas some cells were inhibited. Cells shown in (D_1) are indicated.

Error bars represent SEM.

onto M/T cells (Eyre et al., 2008) and paired-recordings have shown that dSACs generate IPSCs onto GCs (Eyre et al., 2008, 2009; Pressler and Strowbridge, 2006). However, the excitatory inputs governing the activation of dSACs are unclear. We targeted dSACs for recording based on the size of their cell bodies (>10 μm) and their multipolar morphology. Activation of cortical fibers elicited EPSCs with little onset jitter (SD = 0.27 ± 0.04 ms, n = 10; Figure 5A) indicating that, in addition to GCs, dSACs are also a direct target of cortical feedback projections. We next made simultaneous recordings from dSACs synaptically connected to GCs (Figure 3B_1; unitary conductance = 0.8 ± 0.4 nS, n = 6) to probe the contribution of dSACs to cortically-evoked inhibition of GCs. Brief light flashes drove APs in dSACs that coincided with GC IPSCs. Interestingly, on interleaved trials in which the dSAC was hyperpolarized below spike threshold the amplitudes of light-evoked GC IPSCs were strongly attenuated (Figure 3B_2). In all paired recordings, cortically-driven GC IPSCs were significantly smaller when the connected dSAC failed to fire APs (Figure 5B_3; 71.7 ± 9.7% reduction, n = 6, t test, p = 0.03). This suggests that relatively few dSACs contribute to cortically-evoked IPSCs in an individual GC. Furthermore, these results provide strong evidence that dSACs are a major source of the cortically-driven disynaptic inhibition of GCs.

We next considered whether cortical feedback projections preferentially target GCs or dSACs. To address this, we used simultaneous or sequential recordings from dSACs and GCs (within 300 μm) to compare the projections onto these two cell types. Surprisingly, dSACs consistently received stronger excitation than GCs (Figures 5C and 5D). In all paired (12/12) or sequential (5/5) recordings, evoked EPSCs were larger in dSACs than GCs. Similar results were obtained in wild-type mice injected in PCx with an unconditional AAV-ChR2 construct, ruling out the possibility that these differences are unique to projections from Ntsr1-cre pyramidal cells (Figure 5D). On average, the EPSC in dSACs (306 ± 81 pA, n = 17) was ~10 times larger than in GCs (28 ± 9 pA, n = 17). This difference in EPSC amplitude could be due either to stronger unitary connections between cortical fibers and dSACs or a higher convergence of cortical pyramidal cell axons onto dSACs.

To differentiate between these two possibilities, we determined the strength of single fiber connections onto both cell types using minimal optical stimulation. In these experiments, we reduced light intensity to the point at which clear failures of synaptic responses were observed on ≥50% of trials (Figure 5E_1) and we measured the average amplitudes of successes in each cell. The average amplitude of the single-fiber EPSC was actually somewhat larger for inputs onto GCs compared to dSACs (29.8 ± 4.6 pA and 17.0 ± 3.8 pA for GCs (n = 17) and dSACs (n = 10), respectively; K-S test, p = 0.04; Figure 5E_2). Together, these data suggest that dSACs receive stronger excitation than GCs due to a higher convergence of feedback inputs.

Glomerular Layer Targets of Cortical Feedback Projections

In addition to their targets in the GC layer, the presence of cortical fibers in the glomerular layer suggests that additional classes of bulbar neurons receive cortical input. Therefore, we next explored how cortical feedback projections influence circuits in the glomerular layer by studying responses of three major classes of juxtaglomerular cells: principal external tufted (ET) cells, GABAergic superficial short axon cells (sSACs), and

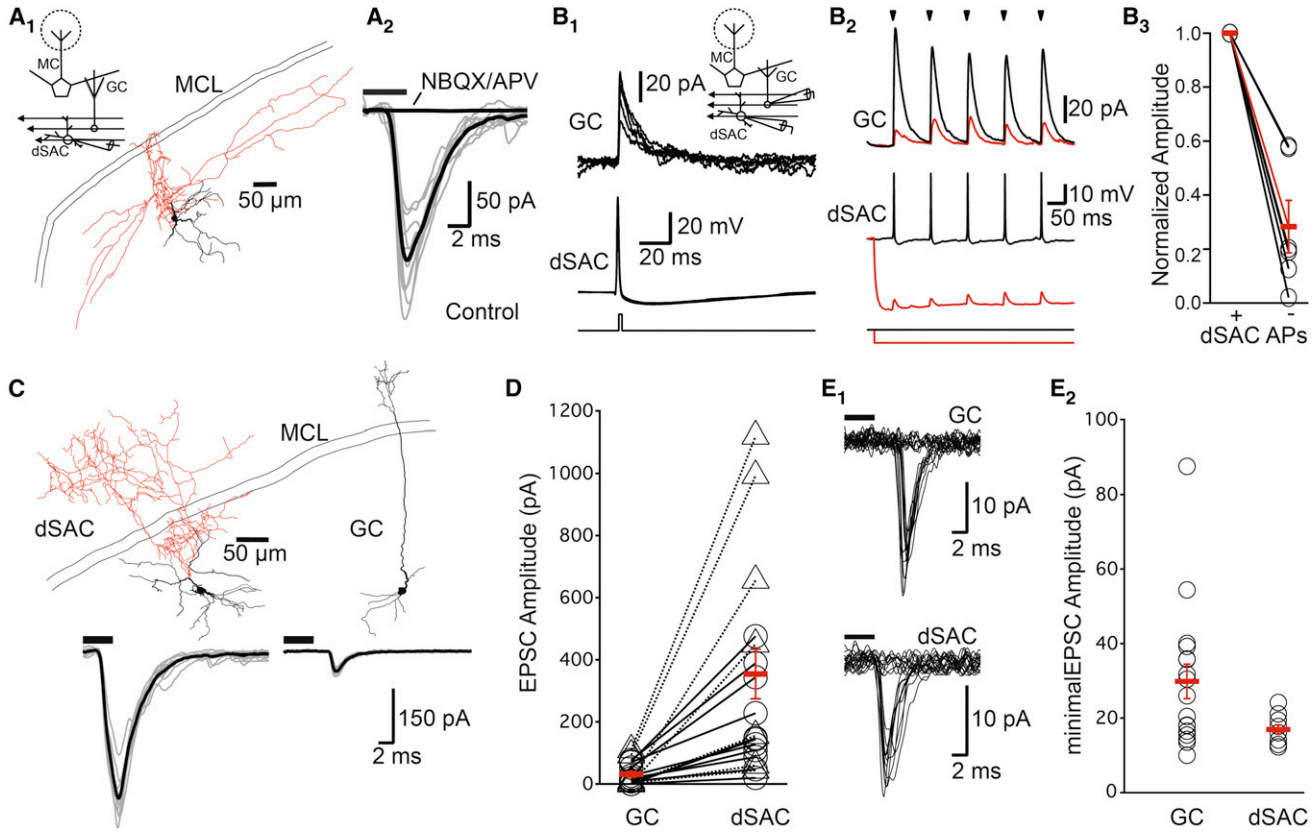

Figure 5. dSACs Mediate Disynaptic Inhibition of GCs and Receive a Higher Convergence of Cortical Feedback Projections

(A_1) Anatomical reconstruction of a dSAC (dendrites in black, axon in red, MCL, mitral cell layer). Inset: recording schematic. (A_2) Light-evoked EPSCs (V_m = −70 mV) from the cell in A_1 before (Control) and after application of NBQX and APV.

(B_1) Simultaneous recording of a connected dSAC-GC pair. A current step triggers an AP in the dSAC (bottom) and a short-latency IPSC in the voltage-clamped GC (V_m = −50 mV). (B_2) Recording from another connected dSAC-GC pair shows GC IPSCs (top, V_m = 0 mV) and dSAC membrane potential (bottom) in response to a train of light flashes (arrowheads). Traces show responses under control conditions (black) and on interleaved trials when hyperpolarizing current was applied to prevent light-evoked APs in the dSAC (red). (B_3) Light-evoked GC IPSCs are consistently smaller when the connected dSAC does not fire spikes (−dSAC APs, n = 6 pairs).

(C) Top: anatomical reconstruction of a simultaneously recorded dSAC and GC. Bottom: light-evoked EPSCs (V_m = −70 mV) are larger in the dSAC than the GC.

(D) Summary showing that light-evoked EPSCs are larger in dSACs than GCs from the same slices. Circles, pairs from Ntsr1-cre animals; triangles, pairs from wild-type animals expressing ChR2 unconditionally. Mean ± SEM shown in red.

(E_1) Minimal optical stimulation of a GC (top) and dSAC (bottom) reveal clear distinction between failures and single-fiber EPSCs (20 traces superimposed, V_m = −70 mV). (E_2) The average single fiber EPSC amplitude (red bar) is similar between the cell types, suggesting dSACs receive a higher convergence of cortical inputs.

Error bars represent SEM.

GABAergic periglomerular (PG) cells. ET cells lack lateral dendrites and receive excitation from olfactory sensory neurons as well as PG cell-mediated dendrodendritic inhibition on their apical dendritic tufts (Gire and Schoppa, 2009; Hayar et al., 2004). Similar to mitral cells, photoactivation of cortical fibers evoked IPSCs onto ET cells with no evidence of direct excitation (n = 6; Figure 6A). Light-evoked inhibition onto ET cells was disynaptic: IPSCs had high onset time jitter (SD = 3.0 ± 0.5 ms, n = 10) and were abolished by glutamate antagonists (APV, 50 µM + NBQX, 10 µM, n = 3, 97 ± 1% reduction). Light flashes elicited fast, monosynaptic EPSCs (onset time SD = 0.31 ± 0.05 ms, n = 10) in PG cells (Figure 6B) that were blocked by NBQX and APV (92 ± 5% reduction, n = 3), suggesting that PG cells are a likely source of disynaptic inhibition onto ET cells. sSACs are characterized by their exclusively periglomerular distribution of dendrites (Pinching and Powell, 1971a; Scott et al., 1987). Although the functional properties and sources of excitatory input to sSACs are not well understood, they are classically proposed to mediate inhibition of PG cells (Pinching and Powell, 1971b). We find that activation of cortical fibers elicits monosynaptic EPSCs (onset time SD = 0.27 ± 0.03 ms) in sSACs (Figure 6C) mediated by glutamate receptors (97 ± 2% block by APV + NBQX, n = 3). Recordings from neighboring (within 100 µm) sSACs (n = 13) and PG cells (n = 13) revealed that sSACs consistently receive stronger cortical input than PG cells (Figure 6D). These findings suggest that cortical feedback could also modulate intra- and interglomerular signaling via inputs to multiple subtypes of glomerular interneurons.

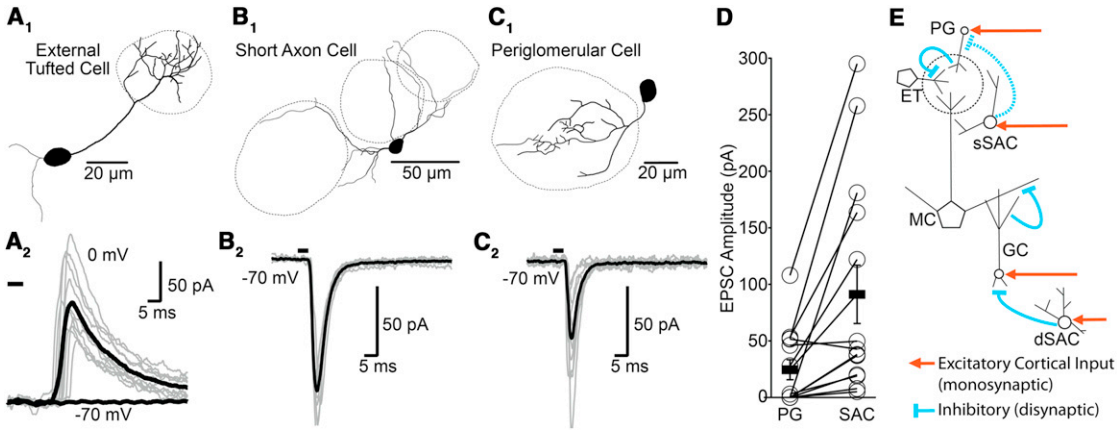

Figure 6. Cortical Feedback Projections Activate Circuits in the Glomerular Layer

(A) Cortical feedback projections drive disynaptic inhibition of external tufted (ET) cells. (A_1) Anatomical reconstruction of an ET cell. (A_2) Voltage clamp recording from the cell in A_1 at −70 mV and 0 mV reveal that activation of cortical fibers elicits IPSCs.

(B) Cortical feedback projections provide direct excitatory input to superficial short axon cells (sSACs). (B_1) Reconstruction of an sSAC. (B_2) Light-evoked EPSCs (−70 mV) from the same cell.

(C) Cortical feedback inputs provide direct excitation to periglomerular (PG) cells. (C_1) Reconstruction of a PG cell. (C_2) Light-evoked EPSCs recorded in voltage clamp (−70 mV) from the same cell.

(D) Recordings from sSAC-PG cell pairs reveal that sSACs receive stronger excitation than PG cells. Bars, mean amplitudes of EPSCs.

(E) Circuit diagram illustrating OB neurons receiving direct excitation (red) and disynaptic inhibition (blue) elicited by cortical feedback projections. Dashed blue line is putative inhibitory connection. GC, granule cell; MC, mitral cell.

Error bars represent SEM.

Photoactivation of Piriform Cortex In Vivo

The diversity of interneurons and local circuits under the control of cortical feedback projections (Figure 6E) make it challenging to predict the role of cortical activity on OB sensory processing. To address this issue, we studied how activation of PCx modulates odor responses in urethane-anesthetized mice.

We first established that we could effectively drive cortical activity in vivo. A craniotomy was performed to expose the ChR2-expressing anterior PCx and we used linear silicon probes to record local field potentials (LFPs) and unit activity. An LED fiber was positioned over the exposed cortical region and a long (4 s) ramping light stimulus was used to drive sustained activation of PCx. We chose this relatively unstructured stimulus because the ramp prevents the fast desensitizing transient of the ChR2 photocurrent and can initiate self-organized rather than externally-defined cortical activity patterns (Adesnik and Scanziani, 2010; Olsen et al., 2012). Consistent with previous findings in layer 2/3 of neocortex (Adesnik and Scanziani, 2010), this photostimulus generated rhythmic oscillation of the PCx LFP at γ frequency (average 52.8 ± 4.3 Hz, n = 5 mice; Figure 7B). LFP γ oscillations were accompanied by an increase in the activity of simultaneously recorded single units, spiking coherently with the LFP at γ frequency (Figure 7C). Furthermore, simultaneous recording of multiunit activity revealed that the light stimulus greatly enhanced AP firing in PCx ($p < 0.005$, t test, n = 5 mice; Figure 7D). Thus, under our conditions, photostimulation of pyramidal cells in layer 2/3 of PCx in vivo strongly increases population activity.

In a subset of experiments, we examined how photoactivation of layer 2/3 pyramidal cells influenced odor-evoked cortical activity. Odors (mixtures of three different monomolecular odorants, applied for 4 s at 30 s intervals) elicited LFP oscillations in both the γ (40–70 Hz) and β (10–30 Hz) frequency ranges (Figure 7E_1). However, when we coapplied odors with the photostimulus, the response resembled that of photostimulation alone: odor-evoked β oscillations were abolished while photo-induced γ oscillations dominated higher frequencies of the LFP (n = 3 mice; Figure 7E_2). Furthermore, coapplication of odors and photostimulation consistently generated more AP firing compared to odors alone ($p < 0.005$, t test, n = 15 odor-animal pairs; Figures 7F and 7G). Thus, photoactivation uniformly increases PCx output both under basal conditions and in the presence of odors.

Driving Cortical Activity In Vivo Amplifies Inhibition in the OB

We next examined how photoactivation of PCx influences responses in the OB. A second craniotomy was made over the OB ipsilateral to the ChR2-expressing PCx and we recorded LFPs and unit activity in the mitral cell layer. We used a protocol in which cortical LED illumination either preceded or coincided with odor application on interleaved trials (Trial A, Trial B) to assess the effects of cortical activation on spontaneous and odor-evoked activity. Intriguingly, cortical photoactivation alone (A trials) caused a marked increase in OB LFP γ oscillations ($p < 0.005$, Holm test, n = 10 odor-animal pairs; Figures 8B_1 and 8B_3). It has been proposed that synchronized reciprocal interactions between M/T and GCs underlie the generation of OB γ oscillations (Rall and Shepherd, 1968). Our results indicate that γ frequency cortical activity propagates to the OB and is sufficient to drive local γ oscillations, presumably by synchronizing GC activity. As in cortex, odors elicited both β and γ oscillations in the LFP under control conditions (A trials, $p < 0.05$, Holm test,

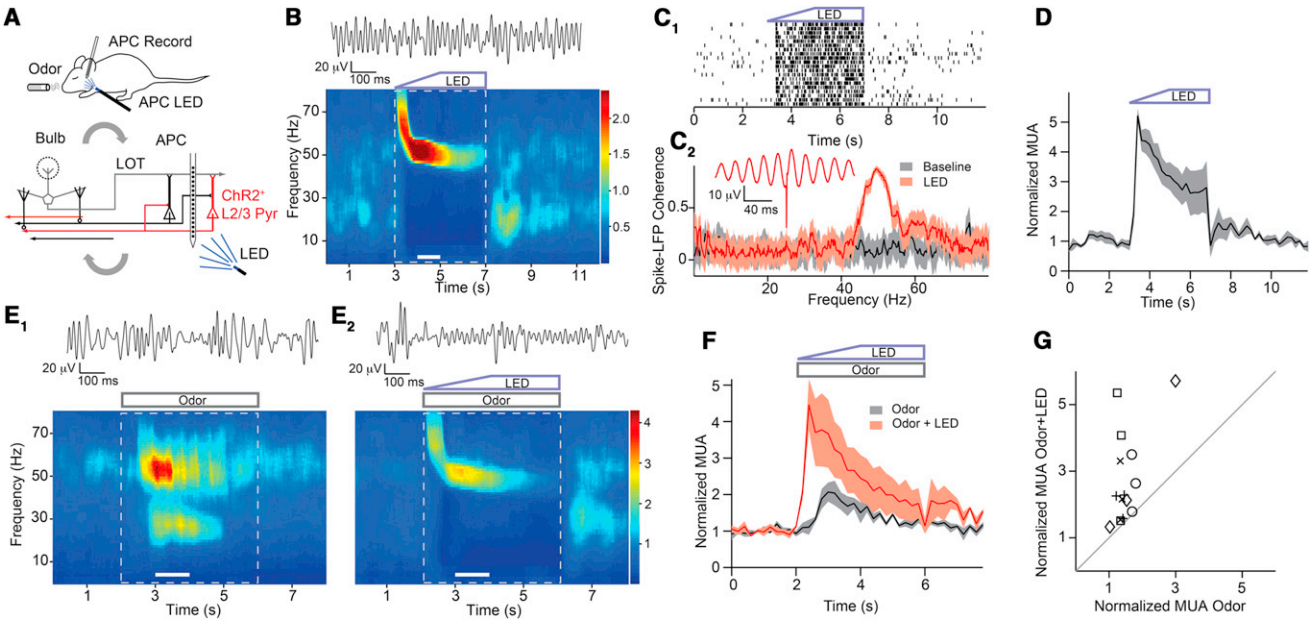

Figure 7. Photoactivation of Pyramidal Neurons Expressing ChR2 In Vivo Drives a Sustained Increase in γ-Synchronized Firing in Piriform Cortex

(A) Recording schematic and circuit diagram. A subset of layer 2/3 neurons express ChR2 (red).

(B) Photoactivation generates γ oscillations. Top: LFP trace during LED illumination. Bottom: average spectrogram (20 trials) from the same experiment. The trapezoid and white box indicate the period of LED illumination. White bar, period from which the trace was derived.

(C) Photoactivation drives γ frequency firing of pyramidal cells. (C_1) Raster plot of light-evoked firing of a single unit. (C_2) Spike-LFP coherence for the same unit during baseline (gray) and LED (red) periods. Shaded regions, 95% confidence intervals. Inset: spike-triggered average LFP.

(D) Summary results show that photostimulation causes a marked increase in AP firing. Pooled histogram of multi-unit activity (MUA), gray shading indicates ±SEM.

(E) Photoinduced cortical γ activity abolishes odor-evoked β oscillations. Representative experiment showing the effects of odor and combined odor + LED stimulation on LFP activity. Example LFP traces (top) and average spectrograms (bottom). White boxes indicate the odor or odor + LED period and white bars the extent of the example LFP traces. Trapezoid and rectangle indicate LED and odor timing, respectively. (E_1) Average spectrogram of LFP activity during odor application alone. (E_2) Average spectrogram of LFP activity during interleaved trials with odor + LED.

(F) Summary results of the effect of photoactivation on firing activity in cortex during odor stimulation. Pooled MUA histogram averaged across odors (n = 3 mice). Normalized activity in response to odors alone (gray) and odors + LED (red) plotted with shaded regions representing ±SEM.

(G) MUA scatter plot of normalized firing rates for odors alone versus odors + LED periods show that photoactivation increases AP output. Symbol shapes correspond to distinct odors (n = 15 odor/animal pairs). Diagonal represents unity line.

n = 10; Figures 8B_1 and 8B_3). While odor-evoked γ oscillations are thought to arise from reciprocal interactions between M/T cells and GCs, lesion studies suggest that β oscillations additionally require a feedback loop involving cortical projections (Gray and Skinner, 1988; Martin et al., 2006; Neville and Haberly, 2003). Consistent with these studies, photostimulation that briefly disrupted odor-evoked β oscillations in the cortex also acutely suppressed β oscillations in the OB (B trials, $p < 0.05$, Holm test, n = 10; Figures 8B_2 and 8B_3).

Surprisingly, multi-unit recordings in the mitral cell layer revealed that cortical photostimulation had differential effects on spontaneous and odor-evoked M/T cell activity. Although spontaneous firing was not significantly affected by cortical activation ($p > 0.05$), odor-evoked firing was consistently reduced ($p < 0.001$, Wilcoxon signed-rank test, n = 15 odor-recording site pairs; Figures 8C_1 and 8C_2). These results demonstrate that, under our conditions, cortical photoactivation preferentially reduces M/T cell population activity during the processing of sensory stimuli implying a synergistic effect between sensory input and cortical activity.

Because multi-unit activity is dominated by neurons with high firing frequencies, we determined the effect of cortical photostimulation on isolated single units whose average firing rates varied over a large range. At the single unit level, M/T cell odor-evoked responses varied from clear excitation (Figure 8D_1) to pure decreases in firing due to lateral inhibition (Figure 8D_2). Cortical photoactivation both reduced odor-evoked increases in firing (Figure 8D_1) and augmented odor-evoked inhibitory responses (Figure 8D_2) in individual cells. The simplest interpretation of these effects is that cortical activation enhances recurrent and/or lateral inhibition. Across the population of M/T cell single units (n = 40 odor-unit pairs, seven mice), cortical photostimulation could both increase and decrease spontaneous firing rate (Figures 8E_1 and S2). In contrast, cortical activation consistently led to decreases in firing rates in the presence of odor stimuli ($p > 0.05$ and $p < 0.001$ for spontaneous and odor-evoked activity respectively, Wilcoxon signed-rank test; Figure 8E_2). To confirm that cortical activity suppressed odor-responses independently of whether odors increased or decreased firing rate, we calculated an odor modulation index

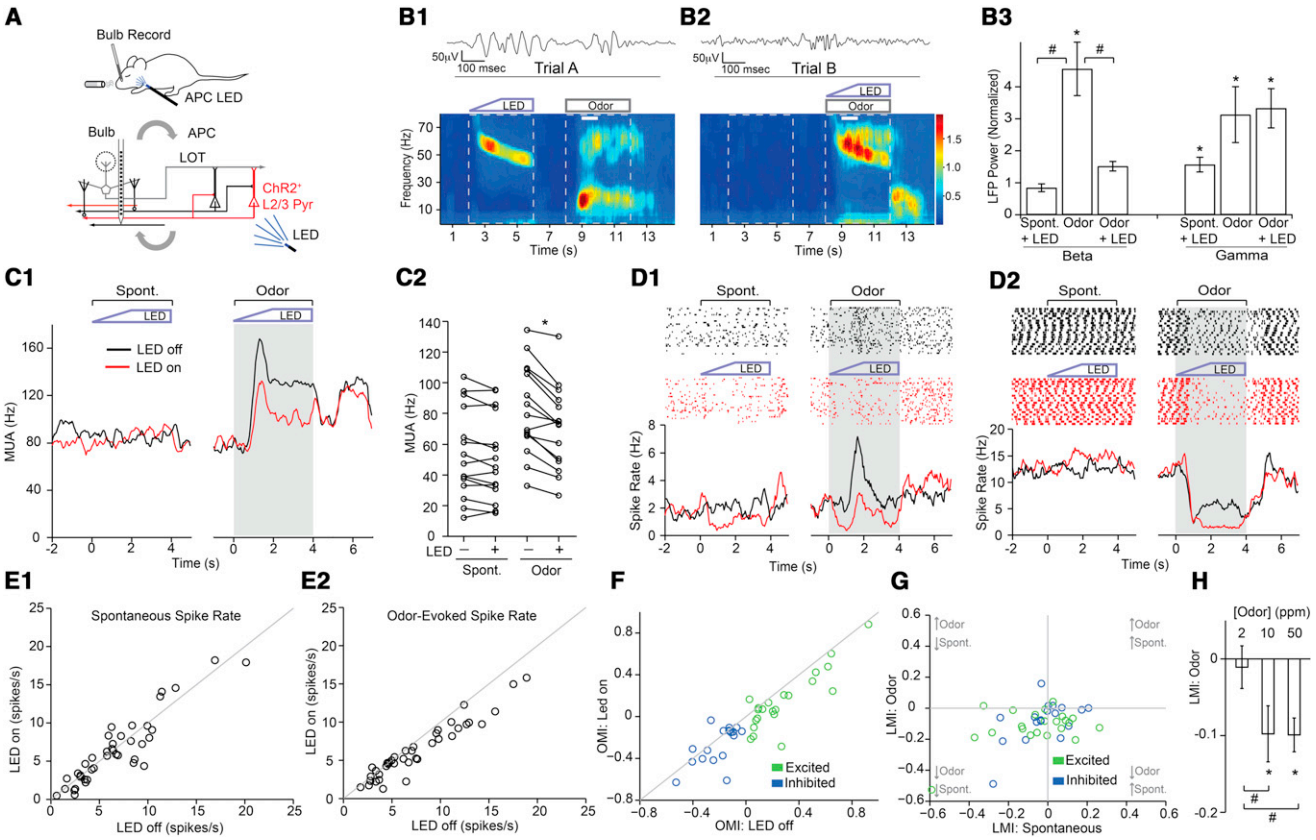

Figure 8. Activation of Piriform Cortex In Vivo Amplifies Odor-Evoked Inhibition in the Olfactory Bulb

(A) Recording schematic and circuit diagram.

(B) Photo-induced γ activity in cortex propagates to the bulb and disrupts β oscillations. On interleaved trials, cortical photostimulation preceded (Trial A) or was coincident (Trial B) with odor application. (B_{1}) Top: LFP trace during odor application. Bottom: average spectrogram when cortical LED illumination (blue trapezoid) preceded odor application (gray box) for Trial A. (B_{2}) Top: LFP trace during coincident cortical photostimulation and odor application. Bottom: average spectrogram when LED illumination was coincident with odor application for Trial B. White bounding boxes represent periods over which spontaneous and odor-evoked LFP activity are calculated and white bars indicate periods used for LFP traces. (B_{3}) Summary results showing that cortical photoinduced γ activity reduces odor-evoked β oscillations. Spectral power in the β (10–30 Hz) and γ (40–70 Hz) bands for the effects of photostimulation alone (Spont. + LED, Trial A), odor alone (Odor, Trial A), and Odor + LED (Trial B). LFP power is normalized to the 4 s period in Trial B when LED and odor stimulation was absent (*$p < 0.05$ relative to control, #$p < 0.05$ for pairwise comparisons).

(C) Cortical photostimulation reduces odor-evoked M/T cell firing but has minimal effects on spontaneous activity. (C_{1}) Example of multi-unit activity from one experiment. Peristimulus time histograms (PSTHs) of firing rate under control conditions (black) and with LED illumination (red) reveal a selective suppression of odor-evoked but not spontaneous firing. (C_{2}) Summary data of multi-unit activity showing that cortical photoactivation had variable effects on spontaneous firing but significantly suppressed odor-evoked activity (*$p < 0.001$).

(D) Recordings from M/T cell single units reveal that cortical photostimulation reduces odor-evoked increases in firing and enhances odor-evoked inhibition. (D_{1}) Odor-activated unit. Top: raster of AP firing on interleaved trials (Trial A, Trial B) are segmented to show spontaneous (left) and odor-evoked activity (right) under control conditions (black) and during photostimulation (red). Trapezoids and gray shading indicating timing of LED and odor stimulation, respectively. Bottom: PSTHs under control conditions (black) and with LED illumination (red). (D_{2}) Odor-inhibited unit.

(E) Raw AP rates of single units with (LED on) and without (LED off) photostimulation (n = 40 units). (E_{1}) LED activation of cortex has variable effects on spontaneous firing. (E_{2}) Cortical activation consistently reduces firing during odor-evoked responses.

(F) Cortical activation suppresses firing rate independent of whether odor-evoked responses were excitatory or inhibitory. Scatter plot of odor modulation index (OMI) for single units. Odor-inhibited (blue, OMI < 0) (n = 18) and excited (green, OMI > 0) (n = 22) units are both affected by cortical stimulation.

(G) Little correlation between the effects of cortical activation on spontaneous and odor-evoked activity. Scatter plot of light modulation index (LMI), calculated for spontaneous and odor periods, quantifying the effect of the LED on firing rates for inhibited (blue) (n = 18) and excited (green) (n = 22) units. Horizontal and vertical gray lines and labels define quadrants categorically.

(H) Suppression of M/T cell responses by cortical activation is sensitive to odor concentration. Average LMI across single units (n = 30) when concentrations of 2, 10, and 50 ppm of a single odor were presented on interleaved trials. (*$p < 0.05$ relative to control, # $p < 0.05$ for pairwise comparisons, error bars represent ± SEM). See also Figure S2.

(OMI) $((R_{odor} - R_{baseline})/(R_{odor} + R_{baseline})$, where R_{odor} = firing rate during 4 s odor application, $R_{baseline}$ = rate during first 2 s of each trial [Eliades and Wang, 2008]) for each odor-cell pair. Thus, OMI measures the relative change in firing rate during odor application compared to baseline conditions and ranges from −1 (complete suppression of activity) to +1 (strongly driven

responses). Indeed, this analysis showed that photostimulation had a suppressive action on odor responses regardless of whether the firing rate of individual odor-cell pairs was increased ($p < 0.001$, $n = 22$) or decreased ($p < 0.05$, $n = 18$) by the odor alone (Wilcoxon signed-rank test; Figure 8F).

We also asked whether there was any relationship between the effects of cortical activation on spontaneous and odor-evoked responses within individual cells. To address this, we calculated a light modulation index (LMI) $((R_{LED} - R_{Control})/(R_{LED} + R_{Control})$, where R_{LED} = average firing rate with photostimulation, $R_{Control}$ = average rate without photostimulation) to compare the relative effects of cortical activation on both spontaneous and odor-evoked firing for each odor-cell pair (LMI ranges from −1 for complete suppression of firing by photostimulation, to +1 indicating strong enhancement of the response). This analysis revealed little correlation ($r = 0.5$, Spearman's correlation coefficient) between the effects of photostimulation on spontaneous activity and responses to odors within individual cells (Figure 8G). However, across the population of M/T cells, the effect of cortical activation on odor-modulated activity was significantly greater than that on spontaneous activity ($p < 0.05$, Wilcoxon signed-rank test). Thus, the effect of cortical feedback on M/T cell activity is context-dependent such that cortical activity preferentially suppresses M/T cell responses during sensory stimulation.

In additional recordings, we considered whether the cortical modulation of M/T cell activity was related to features of the sensory stimulus. We investigated whether the cortical suppression of M/T cell responses depended on odor identity by examining M/T single units tested with three different odors at matched concentrations (50 ppm; Figure S2). Across this cell population ($n = 35$ single units, nine mice), cortical activation significantly suppressed odor-evoked M/T cell activity ($p < 0.001$, Wilcoxon signed-rank test). However, the proportion of M/T cells in which odor responses were selectively modulated (suppression of responses to only one or two of the tested odors versus suppression of responses to all three odors) was not significant (Figure S2). Thus, under our conditions, the effects of cortical feedback on M/T cell responses were not highly specific to particular odors.

We next asked whether the actions of cortical feedback on odor-evoked M/T cell responses depended on odor intensity by examining responses of cells ($n = 30$ single units, 12 mice) to the same odor at three different concentrations. Indeed, we found that cortical stimulation caused a significant suppression of M/T cell activity when odors were applied at concentrations of 10 and 50 ppm ($p < 0.05$), but not when odors were present at a much lower concentration of 2 ppm (Figure 8H). This result is consistent with the idea that the cortical suppression of M/T cell responses depends on sufficient levels of bulbar sensory input. Taken together, these data indicate that cortical feedback regulates sensory information processing in the OB primarily by acting as a gating mechanism that enhances odor-evoked M/T cell inhibition.

DISCUSSION

Here, we use an optogenetic approach to show that cortical feedback projections target diverse populations of interconnected OB interneurons. We show that activation of cortical fibers drives disynaptic inhibition of mitral cells via fast, AMPAR-mediated excitation of GCs. However, activation of cortical fibers also elicits disynaptic feedforward inhibition of GCs and the effects of cortical activity on AP firing in GCs varied from excitation to inhibition. Cortically-evoked inhibition of GCs results from dSACs that receive a higher convergence of inputs from cortical projections than GCs. Despite the potential for opposing actions on interneuron circuits, in vivo recordings reveal that the major effect of activating cortical feedback projections on M/T cells is to accentuate odor-evoked inhibition and reduce AP firing during the processing of sensory input.

Functional Properties of Cortical Feedback Projections

We find that cortical feedback projections elicit mitral cell disynaptic inhibition that differs from classical dendrodendritic inhibition triggered by mitral cell activity. First, while mitral cell recurrent and lateral dendrodendritic inhibition is due to a long-lasting (many hundreds of ms) barrage of asynchronous IPSCs (Isaacson and Strowbridge, 1998; Schoppa et al., 1998; Urban and Sakmann, 2002) activation of cortical fibers evokes short-latency inhibition with a briefer time course (<100 ms). Second, recurrent and lateral dendrodendritic inhibition typically requires the activation of GC NMDARs (Chen et al., 2000; Isaacson and Strowbridge, 1998; Schoppa et al., 1998), while cortically-evoked IPSCs are insensitive to NMDAR antagonists and require AMPAR activation. Our results suggest that GCs are the likely source of cortically-evoked mitral cell inhibition. Cortical projections evoke short latency APs in GCs and fast (<2 ms) EPSCs mediated by Ca^{2+}-impermeable AMPARs. Although NMDARs are also present at GC cortical synapses, AMPAR-mediated transmission is sufficient to drive AP-dependent fast mitral cell inhibition.

We also show that when mitral cells are suprathreshold, fast cortically-driven IPSPs can both transiently suppress mitral cell APs and elicit rebound firing. Previous studies found that while small, brief IPSPs promote rebound spiking in mitral cells, larger hyperpolarizations due to summating IPSPs have a purely inhibitory action (Balu and Strowbridge, 2007; Desmaisons et al., 1999). Thus, cortically-driven IPSPs may exert bidirectional control of mitral cell firing: small, phasic IPSPs could promote synchronization of APs in ensembles of mitral cells by triggering rebound spikes, while stronger IPSPs due to widespread activation of GCs by cortical input could inhibit large ensembles of mitral cells.

In addition to direct excitation, activation of cortical feedback projections evoked short-latency, disynaptic inhibition of GCs. Previous studies have found that dSACs are a heterogeneous class of interneurons that mediate axo-dendritic inhibition of GCs (Eyre et al., 2008, 2009; Pressler and Strowbridge, 2006); however, the sources of excitatory input to dSACs have not been identified. We identified dSACs as the source of cortically-evoked disynaptic inhibition onto GCs and show that individual dSACs integrate excitatory input from a larger population of pyramidal cells than individual GCs. This preferential targeting suggests that dSACs could receive broadly tuned cortical excitation, while GCs receive cortical excitation that is much more odor-selective. One intriguing scenario is that individual GCs

receive cortical input specifically from pyramidal cells whose odor tuning matches that of the reciprocally connected mitral cells.

Why do GCs receive feedforward inhibition from the cortex? In the simplest case, it ensures a brief time window for the integration of excitation. Indeed, while disynaptic inhibition strongly limits the duration of the cortically-evoked EPSP, its peak amplitude is unaffected due to the fast kinetics of the underlying EPSC. Thus, feedforward inhibition should enable GC excitation to be precisely time-locked to cortical input. Surprisingly, we found a marked heterogeneity across GCs in the relative balance of excitation and inhibition evoked by cortical projections. Although most GCs receiving cortically-evoked responses were excited, a smaller fraction responded with net inhibition. This was observed in nearby GCs in which the same fiber population was activated, ruling out that the heterogeneity is simply due to differences in ChR2-expressing axons across experiments. The differences in excitation/inhibition ratio could reflect the fact that the GC population is continually being renewed by postnatal neurogenesis (Lledo et al., 2006). Activity-dependent processes that vary over the different lifetimes of individual cells may modulate the balance of excitatory and inhibitory connections.

In addition to targeting interneurons in the GC layer, we also show that cortical feedback projections influence circuits in the glomerular layer. While ET cells received disynaptic inhibition, cortical fibers produced direct excitation of both sSACs and PG cells. We found that cortical fibers drove stronger excitation of sSACs compared to PG cells, recapitulating the differential connectivity of cortical projections made onto dSACs and GCs. PG cells and ET cells are thought to regulate glomerular excitation via reciprocal dendrodendritic inhibition (Hayar et al., 2004; Murphy et al., 2005) and this intraglomerular circuit is proposed to gate "on/off" signaling from individual glomeruli (Gire and Schoppa, 2009). While the axonal targets and functional role of sSACs is a source of debate (Kosaka and Kosaka, 2011), they are generally thought to provide a mechanism for long-range interglomerular inhibition. Thus, in addition to modulating M/T cell inhibition via GCs, cortical feedback also has the capacity to shape intra- and interglomerular signaling that contributes to M/T cell excitability. Our results are in general agreement with a study showing that feedback projections from another olfactory cortical region, the AON, target diverse types of OB neurons (Markopoulos et al., 2012 [this issue of *Neuron*]). Differences in the functional effects of feedback projections in the two studies suggest that the AON and PCx may preferentially influence different OB circuits.

Optogenetic Stimulation of Piriform Cortex In Vivo

We studied how cortical feedback modifies OB activity in vivo using photoactivation of ChR2-expressing pyramidal cells in anterior PCx. We used a sustained light pulse that induced LFP oscillations and pyramidal cell firing in the γ frequency range. Thus, rather than imposing a particular temporal structure to the cortical stimulus, we let the cortical network dictate its own inherent pattern of activity (γ frequency output) to the OB. In contrast, trains of brief light pulses (like conventional extracellular stimulation) would drive highly synchronous cortical activity entrained to the frequency of the light stimulus. Trying to select optimal stimulation parameters based on their physiological relevance is challenging, however, given that odors drive γ oscillations in the PCx, we think our choice of photostimulus reasonable.

Impact of Cortical Feedback In Vivo

We show that ChR2-mediated depolarization of pyramidal cells generates intrinsic γ activity in the cortex that propagates to the OB and disrupts odor-evoked β oscillations in both brain regions. Odors evoke γ and β frequency LFP oscillations that are synchronous between the PCx and OB (Neville and Haberly, 2003) and the synchronization of neuronal activity during oscillations is suggested to contribute to odor coding (Laurent, 2002). When triggered by odors, γ oscillations appear to originate in the OB and are relayed via the LOT to the cortex, while β oscillations require reciprocal interactions between bulb and cortex (Gray and Skinner, 1988; Martin et al., 2006; Neville and Haberly, 2003). Our results suggest that γ oscillations in the bulb can also arise from feedback projections that convey γ activity intrinsically-generated from the olfactory cortex. It has been proposed that odor-evoked β oscillations could result either from a M/T cell $\rightarrow$ pyramidal cell $\rightarrow$ GC loop or from intrinsic β activity in cortex that is relayed back to the bulb (Neville and Haberly, 2003). Although we cannot exclude the possibility that the PCx could generate intrinsic β oscillations under some conditions, our finding that ChR2-driven depolarization generates intrinsic γ activity are most consistent with the idea that odor-evoked β oscillations result from a feedback loop involving coordinated activity of M/T cells, pyramidal cells, and GCs.

Although activating PCx in vivo under our conditions had variable effects on spontaneous M/T cell activity, it consistently reduced M/T cell firing during odor stimulation. The effects of cortical activation on M/T cell responses were also sensitive to odor concentration, consistent with the notion of a synergistic effect between sensory input and cortical activity. The increases and decreases in spontaneous activity across different M/T cells suggests that cortically-evoked disynaptic inhibition is sufficient to suppress spontaneous firing in some M/T cells, while others show a net increase in firing presumably due to IPSP-triggered rebound spikes or "disinhibition" mediated by dSACs. The major effect of cortical activation on M/T cell odor responses was a reduction in odor-evoked excitation and an enhancement of odor-evoked inhibition. The augmentation of purely inhibitory responses further implies that cortical activity amplifies lateral inhibition during sensory processing in the OB.

Although cortical fibers target multiple classes of interneurons in the OB, we suspect that cortically-driven GC excitation plays a dominant role during odor processing. In brain slices, tetanic stimulation of the GC layer (Chen et al., 2000; Halabisky and Strowbridge, 2003) or anterior PCx (Balu et al., 2007) has been shown to facilitate mitral cell-evoked recurrent and lateral inhibition. Thus, cortical excitatory input onto GC proximal dendrites could contribute to the relief of the Mg^{2+} block of NMDARs at distal dendrodendritic synapses and boost or "gate" inhibition onto mitral cells (Balu et al., 2007; Halabisky and Strowbridge, 2003; Strowbridge, 2009). Our in vivo findings that cortical input preferentially drives OB inhibition during sensory processing are

in good agreement with this gating model. However, we do not rule out a contribution of glomerular layer interneurons to the enhancement of odor-evoked inhibition.

While GC-mediated inhibition contributes to odor discrimination (Abraham et al., 2010), the role of lateral inhibition in odor coding is controversial. Although it has been proposed to sharpen the odor tuning of M/T cells belonging to individual glomeruli in a center-surround fashion (Yokoi et al., 1995), this requires a chemotopic map such that glomeruli that respond to similar odorant features are spatially clustered. However, studies have highlighted the lack of a fine scale glomerular chemotopic map and found that M/T cells are not preferentially influenced by nearby glomeruli (Fantana et al., 2008; Soucy et al., 2009). Rather than exerting local actions, lateral inhibition could underlie a more uniform reduction in the activity of M/T cells across all glomeruli and act as a gain control mechanism (Soucy et al., 2009). Furthermore, even "global" lateral inhibition that reduces activity in all M/T cells such that fewer in total are active could enhance odor discrimination by decorrelating activity patterns (Arevian et al., 2008; Cleland and Linster, 2012; Wiechert et al., 2010).

Our results imply that odor representations in the OB are dynamically regulated by brain state. Although we studied anesthetized mice, in awake and behaving animals higher overall levels of cortical activity should lead to enhanced odor-evoked recurrent and lateral inhibition and an increase in the sparseness of M/T cell odor representations. Thus, cortical feedback is poised to play an important role in shaping the initial stages of odor information processing in the brain.

EXPERIMENTAL PROCEDURES

Viral Injections of Ntsr1-cre Mice

Experiments followed approved national and institutional guidelines for animal use. Ntsr1-cre animals (Tg(Ntsr1-cre)209Gsat) were obtained from the GENSAT Project. The full expression pattern of Cre-recombinase in this line can be viewed at http://www.gensat.org. Cre^+ neurons in olfactory cortex have previously been characterized as layer 2/3 pyramidal neurons (Stokes and Isaacson, 2010).

High-titer (1.2×10^{12}) stock of AAV (2/8) containing pAAV-EF1a-double floxed-hChR2(H134R)-mCherry-WPRE-HGHpA (Addgene 20287) was produced by the Salk Vector Core. Neonatal Ntsr1-cre mice (postnatal day 0–2) were anesthetized and virus injection sites targeting the anterior PCx were determined based on landmarks including the superficial temporal vein and the posterior border of the eye. Injections (23 nl) were made using beveled pipettes (Nanoject II, Drummond) at four injection sites at depths of 0.18–0.25 mm. Although the majority of mice received injections into only one PCx, virus was injected bilaterally into some animals to express ChR2 in cortical projections to both OBs and data from these two groups of animals were pooled.

Slice Recording

Mice (postnatal day 10–30) were anesthetized with isoflurane and decapitated. OBs were removed and placed into ice cold artificial cerebrospinal fluid (aCSF) containing (in mM) 83 NaCl, 2.5 KCl_2, 0.5 $CaCl_2$, 3.3 $MgSO_4$, 1 NaH_2PO_4, 26.2 $NaHCO_3$, 22 glucose, and 72 sucrose, equilibrated with 95% O_2 and 5% CO_2. Coronal or horizontal slices (300–400 μm) were cut using a vibrating slicer and incubated at 35°C for 30 min. Slices were transferred to a recording chamber and superfused with aCSF containing (in mM): 119 NaCl, 2.5 KCl, 2.5 $CaCl_2$, 1.3 $MgSO_4$, 1 NaH_2PO_4, 26.2 $NaHCO_3$, and 22 glucose, equilibrated with 95% O_2 and 5% CO_2. All experiments were conducted at 28°C–30°C.

Patch-clamp recordings were performed using an upright microscope and DIC optics. Neuron types were identified by their morphology, intrinsic properties, and laminar location. For glomerular layer recordings, juxtaglomerular cells were filled with fluorescent dye (Alexa 488, 40 μM) and classified based on morphological and electrophysiological criteria (Hayar et al., 2004; Murphy et al., 2005). ET cells were identified as having large (~20 μm) somata, a single dendrite and tuft ramifying within one glomerulus, an axon extending into the EPL and a relatively low input resistance (197 ± 36 MΩ, n = 10). PG cells were distinguished by their small somata (~10 μm diameter) and high input resistance (~1 GΩ). sSACs were distinguished by their unique dendritic arbors that are exclusively periglomerular, span multiple glomeruli, lack tufts, and are poorly branched. Recordings were made using a Multiclamp 700A amplifier (Molecular Devices) digitized at 10–20 kHz and acquired using AxographX software. For most recordings, pipettes (3–6 MΩ) contained (in mM: 130 D-gluconic acid, 130 CsOH, 5 NaCl, 10 HEPES, 10 EGTA, 12 phosphocreatine, 0.2 spermine, 3 Mg-ATP, and 0.2 Na-GTP [pH 7.3]). For some voltage clamp recordings and all current clamp recordings, a K^+-based internal solution was used (in mM: 150 K-gluconate, 1.5 $MgCl_2$, 5 HEPES buffer, 0.1 EGTA 10 phosphocreatine, and 2.0 Mg-ATP [pH 7.4]). Series resistance was routinely <20 MΩ and continuously monitored. In some experiments biocytin (0.2%) or fluorescent dye (Alexa 488) was added to the pipette to allow for reconstruction of cell morphology (Neurolucida). Voltages were corrected for a junction potential of 15 mV.

A collimated LED light source (455 nm, 210 mW, ThorLabs) or output from a xenon lamp (470 nm, TILL) was directed through the 40× microscope objective for photoactivation of ChR2. Full-field illumination was used unless stated otherwise. In mitral cell recordings, the objective was centered at the midpoint of the GC layer directly below the recorded cell. For all other experiments of neurons in the GC or glomerular layer, illumination was centered over the recorded cell. With full-field illumination, translation of the objective <200 μm did not alter the amplitude of light-evoked responses.

In Vivo Recording

We made recordings from Ntsr1-cre mice (postnatal day 28–60) previously injected in PCx with AAV-ChR2-mCherry (n = 25). In some experiments (n = 3), we expressed ChR2 conditionally by crossing Ntsr1-cre mice with a transgenic ChR2 reporter line (Ai32) (Madisen et al., 2012). We did not see any obvious differences using these two expression systems and results were pooled. Mice were anesthetized with urethane (1.5 g/kg) and chlorprothixene (2 mg/kg). Animals were headfixed using a custom stereotax, and skin overlaying the masseter muscle and a portion of the zygomatic arch was removed. The coronoid and condyloid processes were retracted and the skull overlaying anterior PCx was thinned with a surgical drill. In some experiments, a small craniotomy was made for insertion of the recording probe. In all experiments, a second craniotomy was performed over the OB after carefully thinning the skull in this region. Body temperature was maintained at 35°C–37°C.

Odors were delivered via a computer-controlled olfactometer with a 1 l/min constant flow. Odors were diluted in mineral oil, and further diluted with charcoal-filtered air to achieve 50 ppm, unless otherwise stated. Odors consisted of 3-component mixtures: (1) cis-3-hexen-1-ol, methyl acetate, octanol; (2) acetophenone, eugenol, hexanol; (3) isoamyl acetate, hexanol, 2-heptanone; (4) cineole, phenylethyl alcohol, amyl acetate; (5) heptaldehyde, cyclohexanone, cumene; (6) propyl propionate, citral, (r)-limonene; and (7) isoamyl butyrate, carvone, ethyl tiglate.

Unit and LFP activity was recorded with 16 channel silicon probes (Neuronexus) and a 16 channel amplifier (AM systems) at 20 kHz. Data were digitized (National Instruments) and acquired with a custom software package written in MATLAB (Olsen et al., 2012). For cortical recordings, penetration depths of the tip of the probe were between 500–700 μm. For the bulb, dorsal penetration depths were ~500 μm and both dorsal and ventral recordings from M/T cells were guided by photo-induced field potentials (see below). Respiration was monitored using a piezoelectric strap mounted across the chest of the animal.

LED stimulation of PCx was accomplished using a fiber-coupled LED (470 nm, 20 mW, 1 mm fiber, 0.48 N.A., Doric Lenses). In a subset of experiments, activation of cortex was monitored directly by extracellular recording. Otherwise, a train of three LED flashes (3 ms duration, 50 ms ISI) to the cortex and extracellular recording in the bulb with the linear probe were used to

assess effective stimulation of cortex and guide the probe to the mitral cell layer. Each flash caused a field EPSP that varied in intensity across depth and reversed approximately at the mitral cell layer (Neville and Haberly, 2003) where a band of unit activity from presumptive M/T cells was observed in multichannel recordings. A ramped (9 mW/s), trapezoidal light stimulus was chosen to effectively drive sustained activity in PCx and mitigate sharp transitions in LFP activity produced by an immediate transition to full LED intensity.

Data analysis was performed using MATLAB. Spike sorting was accomplished using a K-means clustering algorithm and spike-sorting package (UltraMegaSort2000, Hill and Kleinfeld). Single units with >20% estimated spike contamination or >20% missing spikes were excluded. Spectral analysis was accomplished using the Chronux package. Spectrograms and power spectra were calculated from the derivative of the corresponding time series to remove the $1/f^2$ trend in spectral power. For spectral analysis of cortical signals, we used a superficial recording site on the probe situated in layer 1. For OB LFP measurements, the deepest channel in the GC layer was chosen for spectral analysis. LFP traces were bandpass filtered at 10–80 Hz.

SUPPLEMENTAL INFORMATION

Supplemental Information includes two figures and can be found with this article online at http://dx.doi.org/10.1016/j.neuron.2012.10.020.

ACKNOWLEDGMENTS

We are indebted to M. Scanziani for helpful discussions and to S. Olsen, H. Adesnik, R. Malinow, and T. Komiyama for advice and encouragement. Supported by NIDCD (R01DC04682, J.S.I.).

Accepted: October 9, 2012
Published: December 19, 2012

REFERENCES

Abraham, N.M., Egger, V., Shimshek, D.R., Renden, R., Fukunaga, I., Sprengel, R., Seeburg, P.H., Klugmann, M., Margrie, T.W., Schaefer, A.T., and Kuner, T. (2010). Synaptic inhibition in the olfactory bulb accelerates odor discrimination in mice. Neuron *65*, 399–411.

Adesnik, H., and Scanziani, M. (2010). Lateral competition for cortical space by layer-specific horizontal circuits. Nature *464*, 1155–1160.

Arevian, A.C., Kapoor, V., and Urban, N.N. (2008). Activity-dependent gating of lateral inhibition in the mouse olfactory bulb. Nat. Neurosci. *11*, 80–87.

Atasoy, D., Aponte, Y., Su, H.H., and Sternson, S.M. (2008). A FLEX switch targets Channelrhodopsin-2 to multiple cell types for imaging and long-range circuit mapping. J. Neurosci. *28*, 7025–7030.

Balu, R., and Strowbridge, B.W. (2007). Opposing inward and outward conductances regulate rebound discharges in olfactory mitral cells. J. Neurophysiol. *97*, 1959–1968.

Balu, R., Pressler, R.T., and Strowbridge, B.W. (2007). Multiple modes of synaptic excitation of olfactory bulb granule cells. J. Neurosci. *27*, 5621–5632.

Briggs, F., and Usrey, W.M. (2008). Emerging views of corticothalamic function. Curr. Opin. Neurobiol. *18*, 403–407.

Cang, J., and Isaacson, J.S. (2003). In vivo whole-cell recording of odor-evoked synaptic transmission in the rat olfactory bulb. J. Neurosci. *23*, 4108–4116.

Chen, W.R., Xiong, W., and Shepherd, G.M. (2000). Analysis of relations between NMDA receptors and GABA release at olfactory bulb reciprocal synapses. Neuron *25*, 625–633.

Cleland, T.A., and Linster, C. (2012). On-center/inhibitory-surround decorrelation via intraglomerular inhibition in the olfactory bulb glomerular layer. Front. Integr. Neurosci. *6*, 5.

Cudeiro, J., and Sillito, A.M. (2006). Looking back: corticothalamic feedback and early visual processing. Trends Neurosci. *29*, 298–306.

Davison, I.G., and Katz, L.C. (2007). Sparse and selective odor coding by mitral/tufted neurons in the main olfactory bulb. J. Neurosci. *27*, 2091–2101.

de Olmos, J., Hardy, H., and Heimer, L. (1978). The afferent connections of the main and the accessory olfactory bulb formations in the rat: an experimental HRP-study. J. Comp. Neurol. *181*, 213–244.

Desmaisons, D., Vincent, J.D., and Lledo, P.M. (1999). Control of action potential timing by intrinsic subthreshold oscillations in olfactory bulb output neurons. J. Neurosci. *19*, 10727–10737.

Eliades, S.J., and Wang, X. (2008). Neural substrates of vocalization feedback monitoring in primate auditory cortex. Nature *453*, 1102–1106.

Eyre, M.D., Antal, M., and Nusser, Z. (2008). Distinct deep short-axon cell subtypes of the main olfactory bulb provide novel intrabulbar and extrabulbar GABAergic connections. J. Neurosci. *28*, 8217–8229.

Eyre, M.D., Kerti, K., and Nusser, Z. (2009). Molecular diversity of deep short-axon cells of the rat main olfactory bulb. Eur. J. Neurosci. *29*, 1397–1407.

Fantana, A.L., Soucy, E.R., and Meister, M. (2008). Rat olfactory bulb mitral cells receive sparse glomerular inputs. Neuron *59*, 802–814.

Gao, Y., and Strowbridge, B.W. (2009). Long-term plasticity of excitatory inputs to granule cells in the rat olfactory bulb. Nat. Neurosci. *12*, 731–733.

Gire, D.H., and Schoppa, N.E. (2009). Control of on/off glomerular signaling by a local GABAergic microcircuit in the olfactory bulb. J. Neurosci. *29*, 13454–13464.

Gray, C.M., and Skinner, J.E. (1988). Centrifugal regulation of neuronal activity in the olfactory bulb of the waking rabbit as revealed by reversible cryogenic blockade. Exp. Brain Res. *69*, 378–386.

Haberly, L.B. (2001). Parallel-distributed processing in olfactory cortex: new insights from morphological and physiological analysis of neuronal circuitry. Chem. Senses *26*, 551–576.

Haberly, L.B., and Price, J.L. (1978). Association and commissural fiber systems of the olfactory cortex of the rat. J. Comp. Neurol. *178*, 711–740.

Halabisky, B., and Strowbridge, B.W. (2003). Gamma-frequency excitatory input to granule cells facilitates dendrodendritic inhibition in the rat olfactory Bulb. J. Neurophysiol. *90*, 644–654.

Hayar, A., Karnup, S., Ennis, M., and Shipley, M.T. (2004). External tufted cells: a major excitatory element that coordinates glomerular activity. J. Neurosci. *24*, 6676–6685.

Hollmann, M., and Heinemann, S. (1994). Cloned glutamate receptors. Annu. Rev. Neurosci. *17*, 31–108.

Isaacson, J.S., and Strowbridge, B.W. (1998). Olfactory reciprocal synapses: dendritic signaling in the CNS. Neuron *20*, 749–761.

Kay, L.M., and Laurent, G. (1999). Odor- and context-dependent modulation of mitral cell activity in behaving rats. Nat. Neurosci. *2*, 1003–1009.

Kosaka, T., and Kosaka, K. (2011). "Interneurons" in the olfactory bulb revisited. Neurosci. Res. *69*, 93–99.

Laurent, G. (2002). Olfactory network dynamics and the coding of multidimensional signals. Nat. Rev. Neurosci. *3*, 884–895.

Lledo, P.M., Alonso, M., and Grubb, M.S. (2006). Adult neurogenesis and functional plasticity in neuronal circuits. Nat. Rev. Neurosci. *7*, 179–193.

Luskin, M.B., and Price, J.L. (1983). The topographic organization of associational fibers of the olfactory system in the rat, including centrifugal fibers to the olfactory bulb. J. Comp. Neurol. *216*, 264–291.

Madisen, L., Mao, T., Koch, H., Zhuo, J.M., Berenyi, A., Fujisawa, S., Hsu, Y.W., Garcia, A.J., 3rd, Gu, X., Zanella, S., et al. (2012). A toolbox of Cre-dependent optogenetic transgenic mice for light-induced activation and silencing. Nat. Neurosci. *15*, 793–802.

Markopoulos, F., Rokni, D., Gire, D.H., and Murthy, V. (2012). Functional properties of cortical feedback projections to the olfactory bulb. Neuron *76*, this issue, 1175–1188.

Martin, C., Gervais, R., Messaoudi, B., and Ravel, N. (2006). Learning-induced oscillatory activities correlated to odour recognition: a network activity. Eur. J. Neurosci. *23*, 1801–1810.

Matsutani, S. (2010). Trajectory and terminal distribution of single centrifugal axons from olfactory cortical areas in the rat olfactory bulb. Neuroscience *169*, 436–448.

Murphy, G.J., Darcy, D.P., and Isaacson, J.S. (2005). Intraglomerular inhibition: signaling mechanisms of an olfactory microcircuit. Nat. Neurosci. *8*, 354–364.

Nakashima, M., Mori, K., and Takagi, S.F. (1978). Centrifugal influence on olfactory bulb activity in the rabbit. Brain Res. *154*, 301–306.

Neville, K.R., and Haberly, L.B. (2003). Beta and gamma oscillations in the olfactory system of the urethane-anesthetized rat. J. Neurophysiol. *90*, 3921–3930.

Nissant, A., Bardy, C., Katagiri, H., Murray, K., and Lledo, P.M. (2009). Adult neurogenesis promotes synaptic plasticity in the olfactory bulb. Nat. Neurosci. *12*, 728–730.

Olsen, S.R., Bortone, D.S., Adesnik, H., and Scanziani, M. (2012). Gain control by layer six in cortical circuits of vision. Nature *483*, 47–52.

Petreanu, L., Mao, T., Sternson, S.M., and Svoboda, K. (2009). The subcellular organization of neocortical excitatory connections. Nature *457*, 1142–1145.

Pinching, A.J., and Powell, T.P. (1971a). The neuron types of the glomerular layer of the olfactory bulb. J. Cell Sci. *9*, 305–345.

Pinching, A.J., and Powell, T.P. (1971b). The neuropil of the periglomerular region of the olfactory bulb. J. Cell Sci. *9*, 379–409.

Pouille, F., and Scanziani, M. (2001). Enforcement of temporal fidelity in pyramidal cells by somatic feed-forward inhibition. Science *293*, 1159–1163.

Pressler, R.T., and Strowbridge, B.W. (2006). Blanes cells mediate persistent feedforward inhibition onto granule cells in the olfactory bulb. Neuron *49*, 889–904.

Rall, W., and Shepherd, G.M. (1968). Theoretical reconstruction of field potentials and dendrodendritic synaptic interactions in olfactory bulb. J. Neurophysiol. *31*, 884–915.

Rubin, B.D., and Katz, L.C. (1999). Optical imaging of odorant representations in the mammalian olfactory bulb. Neuron *23*, 499–511.

Schoppa, N.E., Kinzie, J.M., Sahara, Y., Segerson, T.P., and Westbrook, G.L. (1998). Dendrodendritic inhibition in the olfactory bulb is driven by NMDA receptors. J. Neurosci. *18*, 6790–6802.

Scott, J.W., McDonald, J.K., and Pemberton, J.L. (1987). Short axon cells of the rat olfactory bulb display NADPH-diaphorase activity, neuropeptide Y-like immunoreactivity, and somatostatin-like immunoreactivity. J. Comp. Neurol. *260*, 378–391.

Shepherd, G.M., Chen, W.R., and Greer, C.A. (2004). Olfactory bulb. In The Synaptic Organization of the Brain, G.M. Shepherd, ed. (New York: Oxford University Press), pp. 165–216.

Shipley, M.T., and Adamek, G.D. (1984). The connections of the mouse olfactory bulb: a study using orthograde and retrograde transport of wheat germ agglutinin conjugated to horseradish peroxidase. Brain Res. Bull. *12*, 669–688.

Soucy, E.R., Albeanu, D.F., Fantana, A.L., Murthy, V.N., and Meister, M. (2009). Precision and diversity in an odor map on the olfactory bulb. Nat. Neurosci. *12*, 210–220.

Stokes, C.C., and Isaacson, J.S. (2010). From dendrite to soma: dynamic routing of inhibition by complementary interneuron microcircuits in olfactory cortex. Neuron *67*, 452–465.

Strowbridge, B.W. (2009). Role of cortical feedback in regulating inhibitory microcircuits. Ann. N Y Acad. Sci. *1170*, 270–274.

Uchida, N., Takahashi, Y.K., Tanifuji, M., and Mori, K. (2000). Odor maps in the mammalian olfactory bulb: domain organization and odorant structural features. Nat. Neurosci. *3*, 1035–1043.

Urban, N.N., and Sakmann, B. (2002). Reciprocal intraglomerular excitation and intra- and interglomerular lateral inhibition between mouse olfactory bulb mitral cells. J. Physiol. *542*, 355–367.

Wiechert, M.T., Judkewitz, B., Riecke, H., and Friedrich, R.W. (2010). Mechanisms of pattern decorrelation by recurrent neuronal circuits. Nat. Neurosci. *13*, 1003–1010.

Yokoi, M., Mori, K., and Nakanishi, S. (1995). Refinement of odor molecule tuning by dendrodendritic synaptic inhibition in the olfactory bulb. Proc. Natl. Acad. Sci. USA *92*, 3371–3375.